

Article

A Two-Terminal Directional Protection Method for HVDC Transmission Lines of Current Fault Component Based on Improved VMD-Hilbert Transform

Shuhao Liu , Kunlun Han ^{*}, Hongzheng Li, Tengyue Zhang and Fengyuan Chen

Guangxi Key Laboratory of Power System Optimization and Energy Technology, Guangxi University, Nanning 530000, China; 2112392053@st.gxu.edu.cn (S.L.); 2112392040@st.gxu.edu.cn (H.L.)

^{*} Correspondence: hankl@gxu.edu.cn

Abstract: The traveling wave protection of high voltage direct current (HVDC) transmission lines is susceptible to the influence of transition resistance. As a backup protection, current differential protection has absolute selectivity, but usually requires an increase in delay to avoid misoperation caused by distributed capacitance on the line, resulting in a longer action time. Based on this, a two-terminal directional protection method for HVDC transmission lines is proposed based on Sparrow Search Algorithm (SSA)-Variational Mode Decomposition (VMD) and Hilbert phase difference. On the basis of analyzing the directional characteristics of the current fault component at both ends of the rectifier and inverter sides under different faults, SSA is first used to optimize the parameters of VMD. The residual components representing the direction of the current fault component at both ends are extracted through VMD, and then the Hilbert phase difference of the residual components at both ends is calculated to identify faults inside and outside the line area. In addition, fault pole selection can be achieved based on the ratio of the sum of multi-band Hilbert energy of single-terminal voltage fault components at the positive and negative poles. Simulation experiments have shown that the proposed protection scheme can quickly and effectively identify fault and has good tolerance to transition resistance and noise interference.



Citation: Liu, S.; Han, K.; Li, H.; Zhang, T.; Chen, F. A Two-Terminal Directional Protection Method for HVDC Transmission Lines of Current Fault Component Based on Improved VMD-Hilbert Transform. *Energies* **2023**, *16*, 6987. <https://doi.org/10.3390/en16196987>

Academic Editors: Lin Zhu and Zhigang Wu

Received: 7 September 2023

Revised: 27 September 2023

Accepted: 1 October 2023

Published: 7 October 2023

Keywords: HVDC; current and voltage fault components; Sparrow Search Algorithm; Variational Mode Decomposition; Hilbert transform; fault identification

1. Introduction

HVDC transmission has the advantages of long transmission distance, large transmission capacity, low line loss, and easy control, which is of great significance for large-scale consumption of renewable energy and the realization of rational allocation of resources in a wide area [1,2]. The DC transmission line is long, the protection device is complex, the fault occurrence rate is high, and the reliable and rapid identification of faults plays a vital role in the safe and stable operation of the whole system. Therefore, research on DC line protection is particularly important [3,4].

Current differential protection, as a backup protection for DC line traveling wave protection and differential undervoltage protection [5–7], is mainly used to detect high-resistance grounding faults. Affected by the distributed capacitance of the line, the protection action time can reach up to 1100 ms [8]. In order to improve the sensitivity and rapidity of backup protection, some experts and scholars have conducted extensive research on the time-frequency analysis method for two-terminal electrical quantities protection. Li et al. [9] constructed a two-terminal protection based on the difference in wavelet energy relative entropy of the voltage and current fault components at both ends during internal and external faults, which was difficult to select the basis function of the wavelet transform, and false spectra might appear during decomposition. Shu et al. [10] proposed a protection method based on Principal Component Analysis



Copyright: © 2023 by the authors. Licensee MDPI, Basel, Switzerland. This article is an open access article distributed under the terms and conditions of the Creative Commons Attribution (CC BY) license (<https://creativecommons.org/licenses/by/4.0/>).

(PCA) clustering to determine the direction of short circuit faults. Gong et al. [11]. used the terahertz simulation signals processed by PCA downscaling as samples for Elman neural network training to measure the thickness of aero-generator thermal barrier coatings for determining the faults of its thermal cross-section parts. However, the method was sensitive to data distribution, easily affected by outliers, weakly capable of handling complex nonlinear information, and required a sufficient number of samples for clustering accuracy [12], which remained to be explored for wider application in DC line fault identification. Qi et al. [13] analyzed the polarity difference between the fault voltage and current at both ends of the fault by Hilbert-Huang transform, which was more accurate for fault classification. Nevertheless, the method took Empirical Mode Decomposition (EMD) for transient quantities, ignoring the problems of different degrees of modal aliasing and end-point effects that may occur during signal decomposition [14,15], which limited its fault information extraction performance.

In 2014, Dragomiretskiy and Zosso proposed a novel adaptive, fully non-recursive Variational Mode Decomposition (VMD) algorithm based on a recursive model of the EMD algorithm [16]. VMD decomposes multi-component signals into multiple amplitude modulated-frequency modulated (AM-FM) signals by solving a variational constrained model. It is widely used in medical, mechanical, and signal processing [17–19], and is often used for fault identification and fault location in engineering fields. Viswanath et al. [20] introduced the VMD algorithm in power signal processing, accurately identifying pulse transients and spike signals in the signal. Wang et al. [21] proposed a novel method combining the VMD algorithm and a Teager energy operator for fault location of hybrid DC lines, which outperformed existing time-frequency analysis methods such as Wavelet Transform (WT) and Ensemble Empirical Mode Decomposition (EEMD). Xu et al. [22] discussed the effectiveness of the VMD algorithm in extracting fault information and decomposed multiple power quality disturbance waveforms to extract their feature information. Luo et al. [23] detected and analyzed the ripple components of complex DC signals by a combination of VMD and Hilbert transform. Compared with the EMD algorithm, the VMD algorithm detected more accurately under noisy conditions. In order to improve the fault location accuracy, Wang et al. [24] introduced the VMD feature quantity into a kind of fault location model based on a deep hybrid Convolutional Neural Network (CNN) and a Long Short-Term Memory (LSTM) network, which effectively improved the learning effect of the model.

The combination of VMD and Hilbert transform is a kind of adaptive time-frequency analysis method based on the improvement of the Hilbert-Huang transform [25], which overcomes the problem of large computational errors for the Hilbert transform caused by the error of EMD modal components. It can perform the Hilbert transform on each single-component modal signal decomposed by VMD and extract the fault eigenvalues, and it has been widely used in signal analysis of the power system. Paternina et al. [26] introduced VMD to identify the electromechanical oscillation mode by using the instantaneous modal eigenvalues of the oscillating power signals obtained by the Hilbert transform. In order to reduce the photovoltaic power fluctuation rate under different weather conditions, Xiao et al. [27] used the VMD-Hilbert transform to adaptively allocate the power from the hybrid energy storage system (HESS) to lead-carbon batteries and supercapacitors. Zhang et al. [28] took VMD to conduct feature analysis on the fault transient signal of the positive sequence current, extracted the fault feature vectors through Hilbert transformation, and used them as the input of CNN to establish a fault diagnosis model. Based on a large number of studies, it is found that the number of modal components K and the quadratic penalty factor α of the VMD algorithm have a great influence on the results. However, since the parameters of the VMD algorithm are mostly selected by relying on experience, too much deviation in the parameter selection can lead to distortion of the decomposition results and extraction of inaccurate fault information.

In this paper, a novel two-terminal directional protection method for HVDC transmission lines of current fault component based on improved VMD-Hilbert transform is proposed according to the directional characteristics of the current fault component at both ends of the line. First, the SSA optimization algorithm is used to optimize the two key parameters of VMD by taking the average envelope entropy of the modal components after the decomposition of the original signal as the objective function. Subsequently, the line protection criterion is constructed from the Hilbert phase angle difference of the current fault component at both ends by the VMD-Hilbert transform. Meanwhile, the ratio of the sum of multi-band Hilbert energy of single-terminal voltage fault components at the positive and negative poles are utilized for the fault pole selection. Finally, a simulation model of the Yunnan-Guangzhou ± 800 kV ultra-HVDC transmission line is constructed in PSCAD/EMTDC, and the feasibility of the protection scheme is verified under different fault types. Simulation results show that the proposed scheme can correctly identify the faults inside and outside the HVDC line area without the influence of distributed capacitance and the limitation of fault and has good tolerance to transition resistance and noise interference, which is an excellent novel method for time-frequency analysis.

2. Basic Principles of Improving VMD-Hilbert Transform

2.1. Algorithmic Principles of the VMD-Hilbert Transform

VMD is a signal processing algorithm with high resolution and strong robustness, which essentially involves multiple adaptive Wiener filtering groups. The original signal f is decomposed into K intrinsic mode function (IMF) components with independent center frequency in different frequency bands. The mathematical model for variational mode decomposition is

$$\begin{cases} \text{s.t. } \sum_{k=1}^K \mu_k = f \\ \min_{\{\mu_k\}, \{\omega_k\}} \left(\sum_{k=1}^K \left\| \partial_t \left(\left(\delta(t) + \frac{j}{\pi t} \right) * \mu_k(t) \right) e^{-j\omega_k t} \right\|_2^2 \right) \end{cases} \quad (1)$$

where f is the original signal; K is the number of modal components; μ_k is the k -th IMF component decomposed by VMD; ω_k is the center frequency of the k -th IMF component; $\delta(t)$ is the unit pulse function; and $\|\cdot\|_2^2$ represents L_2 norm operation.

In order to solve the above variational equation, a quadratic penalty factor α and the Lagrange multiplication operator λ are introduced so as to transform Formula (1) into an unconstrained variational problem, whose calculation formula is

$$\begin{aligned} L(\{\mu_k\}, \{\omega_k\}, \{\lambda\}) &= \alpha \sum_{k=1}^K \left\| \partial_t \left(\left(\delta(t) + \frac{j}{\pi t} \right) * \mu_k(t) \right) e^{-j\omega_k t} \right\|_2^2 + \\ &\quad \left\| f(t) - \sum_{k=1}^K \mu_k(t) \right\|_2^2 + \left\langle \lambda(t), f(t) - \sum_{k=1}^K \mu_k(t) \right\rangle \end{aligned} \quad (2)$$

where $\langle x, y \rangle$ represents the inner product of x and y .

The alternating direction multiplier iterative algorithm can be used to iteratively update μ_k and ω_k to find the optimal solution of the constrained variational model, where n is the number of iterations and the update expression is as follows

$$\mu_k^{n+1}(\omega) = \frac{f(\omega) - \sum_{i < k} \mu_i^{n+1}(\omega) - \sum_{i > k} \mu_i^{n+1}(\omega) + \frac{\lambda^n(\omega)}{2}}{1 + 2\alpha(\omega - \omega_k^n)^2} \quad (3)$$

$$\omega_k^{n+1} = \frac{\int_0^\infty \omega |\mu_k^{n+1}|^2 d\omega}{\int_0^\infty |\mu_k^{n+1}|^2 d\omega} \quad (4)$$

Setting the determination accuracy to terminate the iterative update, the $\mu_k(\omega)$ Fourier inverse transform after the completion of the VMD algorithm is $\mu_k(t)$, which can be used to solve for the K IMF components, and then Hilbert transform them to obtain

$$y(t) = \frac{1}{\pi} \int_{-\infty}^{\infty} \frac{\mu_k(\tau)}{t - \tau} d\tau \quad (5)$$

where $y(t)$ is derived from the convolution of $\mu_k(t)$ and $1/t$. In order to better show the local features of the signal, the analytic function $z(t)$ is constructed as

$$z(t) = \mu_k(t) + jy(t) = \beta(t)e^{j\theta(t)} \quad (6)$$

The instantaneous amplitude $\beta(t)$, instantaneous phase angle $\theta(t)$, and instantaneous angular frequency $\omega(t)$ of the analytic function $z(t)$ are, respectively

$$\beta(t) = \sqrt{\mu_k(t)^2 + y(t)^2} \quad (7)$$

$$\theta(t) = \arctan \frac{y(t)}{\mu_k(t)} \quad (8)$$

$$\omega(t) = \frac{d\theta(t)}{dt} \quad (9)$$

From this, another expression for the original signal $f(t)$ can be derived as

$$f(t) = \operatorname{Re} \left(\sum_{k=1}^{K-1} \beta_k(t) e^{j \int \omega_k d\omega} + r_K(t) \right) \quad (10)$$

where Re denotes taking the real part; $\beta_k(t)$ and $\omega_k(t)$ are the instantaneous amplitude and instantaneous angular frequency of the k -th IMF component, respectively, and $r_K(t)$ is the residual component.

Omitting the residual components, the Hilbert spectrum $H(\omega, t)$ reflecting the time-frequency distribution of the signal amplitude can be obtained as

$$H(\omega, t) = \operatorname{Re} \sum_{k=1}^{K-1} \beta_k(t) e^{j \int \omega_k d\omega} \quad (11)$$

Given that the Hilbert transform can accurately extract the amplitude information of the signal at different frequencies, the Hilbert instantaneous energy $E(t)$ of the signal in any frequency band and its Hilbert energy sum E can be obtained as

$$E(t) = \int_{\omega_1}^{\omega_2} H^2(\omega, t) d\omega \quad (12)$$

$$E = \int_{t_1}^{t_2} E(t) dt \quad (13)$$

where ω_1 and ω_2 are the angular frequencies; t_1 and t_2 are the starting and ending moments of the fault sampling time, respectively; $E(t)$ is the Hilbert energy as a function of time in a certain frequency band; E is the sum of Hilbert energies during the fault sampling time in a certain frequency band.

2.2. Parameter Optimization of the VMD Algorithm

In practice, the VMD algorithm first selects the appropriate number of modal components K and the quadratic penalty factor α . Determining the values of K and α only empirically results in a certain bias in the decomposition results. If K is set too small, it will cause incomplete decomposition and produce modal aliasing, and if K is too large, it

will lead to over-decomposition and produce useless spurious components. The quadratic penalty factor α determines the bandwidth of the IMF for each modal component. If α is set too small, it will cause the IMF component bandwidth to be too large and cause overlapping between components, and if α is too large, it will cause the IMF component bandwidth to be too small resulting in the loss of some signal details. Sparrow Search Algorithm (SSA) is a population intelligence optimization algorithm based on the study of sparrow foraging and anti-predation [29], which has a better performance in convergence speed, accuracy and optimality searching ability and is easy to implement compared to Genetic Algorithm (GA) [30], Particle Swarm Optimization (PSO) [31], Differential Evolutionary (DE) Algorithm [32], etc. In order to be able to accurately find the optimal combination of (K, α) , this paper applies SSA to the VMD algorithm for parameter optimization, and its computational principle is shown below.

Discoverers in SSA will constantly search for food to expand their search scope, and their location updates are as follows

$$x_{ih}^{l+1} = \begin{cases} x_{ih}^l \cdot \exp\left(\frac{-i}{\gamma \cdot P}\right), & R_2 < S_t \\ x_{ih}^l + QL, & R_2 \geq S_t \end{cases} \quad (14)$$

where l is the current iteration number; P is the maximum iteration number; x_{ih}^l is the i -th sparrow of dimension h at the l -th iteration; γ is a random number of $(0, 1)$; R_2 is the alarm value; S_t is the iteration target value of $[0.5, 1]$; Q is a random number obeying a normal distribution; and L is a $1 \times h$ matrix with all its elements 1.

The position of the follower in the SSA is updated as follows

$$x_{ih}^{l+1} = \begin{cases} Q \cdot \exp\left(\frac{x\omega_h^l - x_{ih}^l}{i^2}\right), & i > \frac{n}{2} \\ xb_h^{l+1} + |x_{ih}^l - xb_h^{l+1}|A^+ \cdot L, & i \leq \frac{n}{2} \end{cases} \quad (15)$$

where n is the number of sparrows; $A^+ = A^T(AA^T)^{-1}$, and A is a $1 \times h$ matrix randomly set to 1 or -1 ; $x\omega_h^l$ is the worst position of the sparrow in the h -th dimension at the l -th iteration of the population; and xb_h^{l+1} is the optimal position of the sparrow in the h -th dimension at the $(l+1)$ -th iteration of the population.

The initial locations of the alarms are randomly generated, typically representing 10–20% of the total sparrow population, and their locations are updated as follows

$$x_{ih}^{l+1} = \begin{cases} xb_h^l + \eta(x_{ih}^l - xb_h^l), & f_i \neq f_g \\ x_{ih}^l + J \left| \frac{x_{ih}^l - x\omega_h^l}{|f_i - f_w| + e} \right|, & f_i = f_g \end{cases} \quad (16)$$

where η is a step control parameter; J is a random number of $[-1, 1]$; e is a minimal constant; f_i is the fitness value of the i -th sparrow, f_g and f_w are the optimal and worst fitness values of the current sparrow population, respectively.

The average envelope entropy is used as a fitness function to evaluate whether the optimization result is optimal, specifically referring to the average value of the envelope entropy of each modal component obtained by the VMD after decomposing the signal under the parameter combination (K, α) , which represents the sparse characteristics of the original signal. The smaller the average envelope entropy represents, the richer the embedded signal information and the better the decomposition effect. The calculation formula is as follows

$$(\hat{K}, \hat{\alpha}) = \underset{(n,P)}{\operatorname{argmin}} \left(\frac{1}{K} \sum_{k=1}^K S_k \right) \quad (17)$$

where \hat{K} and \hat{a} are the optimal parameter combinations; S_k is the envelope entropy of each modal component after Hilbert demodulation; $S_k(i)$ is calculated as follows

$$S_k(i) = -\sum_{i=1}^N p(i) \log_2[p(i)] \tag{18}$$

$$p_i = c(i) / \sum_{i=1}^N c(i) \tag{19}$$

where $i = 1, 2, \dots, N$, N is the number of sampling points; $p(i)$ is the normalized form of $c(i)$; $c(i)$ is the envelope signal after the original signal is Hilbert transformed.

3. DC Line Fault Discrimination Based on an Improved VMD-Hilbert Transform

For conventional current differential protection, the protection can only operate when the local pole line fault enters the steady state phase. During the fault transient process, the amount of current mutation at both ends of the line has an obvious difference in direction characteristics. Fault direction information can be extracted using time-frequency analysis to realize fault discrimination before control system action. For the above analysis, a DC line protection method based on an improved VMD-Hilbert transform is proposed.

3.1. Analysis of the Direction Characteristics of the Current Fault Component

In this paper, a positive DC line is used as an example, and its simplified equivalent circuit is replaced by a centralized parametric model that takes into account the effect of capacitive currents. When an in- and out-of-area fault occurs on a DC line, the voltage drop at the fault point is equivalent to superimposing a negative voltage source at the fault point, and the fault-attached network is shown in Figure 1. In Figure 1, Z_l and C_{eg} are DC line equivalent impedance and ground equivalent capacitance; Z_f , Z_s , and Z_c are the DC filter, the leveling reactor, and converter equivalent impedance; u_f is the equivalent additional voltage source voltage at the fault point; Δi_R and Δi_I are the rectifier side and inverter side of the current fault component during the fault, and uniformly stipulate that the positive direction of the current is from the busbar to the line.

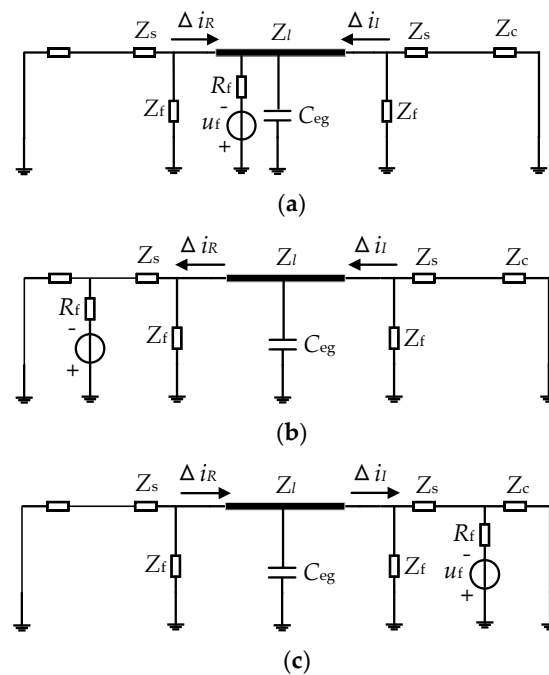


Figure 1. Fault component networks for different fault locations on the HVDC line. (a) Fault inside the line area; (b) External fault on the rectifier valve side; (c) External fault on the inverter valve side.

It can be seen from Figure 1 that when there is an internal fault in the line area, under the action of the fault equivalent additional voltage source, the current fault component Δi_R and Δi_I at both ends flows from the bus to the line, and both directions are the same, both are positive, $\Delta i_R > 0$, $\Delta i_I > 0$; when there is an external fault on the rectifier valve side, also under the action of the fault equivalent additional voltage source, the direction of the rectification side current fault component Δi_R is pointing to the bus, and the direction of the inverter side current fault component Δi_I is pointing to the line, and both directions are opposite, $\Delta i_R > 0$, $\Delta i_I < 0$; when there is an external fault on the inverter valve side also under the action of the fault equivalent additional voltage source, the direction of the current fault component Δi_R on the rectifier side is pointing to the line, and the direction of the current fault component Δi_I on the inverter side is pointing to the bus, and both directions are opposite, $\Delta i_R < 0$, $\Delta i_I > 0$. The analysis of bipolar inter-pole short circuits and AC bus external faults is similar and will not be repeated. Therefore, the use of the direction characteristics of the current fault component at both ends of the line can be used for the identification of faults inside and outside the DC line area.

3.2. SSA-VMD Extraction of Residual Components

When a fault occurs on a DC line, the waveform of the current fault component often does not vary smoothly and monotonically. Due to the significant difference in the oscillation frequency of the fault current at the beginning and end of the line, as well as the distributed capacitance and channel noise of the line, the polarity difference of the current sudden variable fluctuates, making it difficult to effectively characterize the trend of signal changes. However, the VMD algorithm is able to adaptively smooth non-stationary signals based on the local variation characteristics of the signal, effectively filtering out the volatility. According to the theory in Section 2.1, the original signal $f(t)$ is decomposed into the superposition of various IMF components and residual components, with the expression as follows

$$f(t) = \sum_{k=1}^{K-1} \mu_k(t) + r_K(t) \quad (20)$$

where $\mu_k(t)$ is the IMF component of each order arranged from high frequency to low frequency, reflecting the volatility of the current fault component; the residual component $r_K(t)$ characterizes the average trend of the signal, reflecting the direction of change of the current fault component.

Optimization of the parameters of the VMD algorithm using SSA according to different fault types, respectively, the optimal parameter combinations (\hat{K} , $\hat{\alpha}$) can be obtained for different fault types. The number of the sparrow population is set to 80, the maximum number of iterations is 20, and the upper and lower limits of K and α are [3, 20] and [20, 2500], respectively. Figure A1 of Appendix A shows the adaptive curve for optimization of the parameters of the current fault component at both ends of the line during an internal fault in the DC line, which basically reaches stability after three iterations, and the optimal values of the adaptivity function are 3.7389 and 4.165, respectively. Some of the optimal parameter combinations for different fault types after optimization are shown in Table 1.

The VMD parameters are optimized to decompose the current mutation at both ends of the line during faults inside and outside the line area, and the fault moment is set to be $t = 0.6$ s, the time window length is 10 ms, and the sampling frequency is 20 kHz. The VMD decomposition of the current fault component at both ends of the line for an internal fault 400 km from the rectifier side (transition resistance of 100 Ω) and an external fault on the rectifier valve side (transition resistance of 10 Ω) are given in Figure 2, respectively. The residual components $r_R(t)$ and $r_I(t)$ at the ends of the rectifier and inverter sides can reflect the direction of change of the current fault component. As can be seen from Figure 2, the waveforms of each modal component decomposed by the VMD are clear, both high-frequency and low-frequency components are accurately decomposed, and the extracted residual components are monotonic.

Table 1. Parameter optimization under different fault types.

Type of Fault	Fault Distance/km	Transition Resistance/ Ω	Rectifier Side ($\hat{K}, \hat{\alpha}$)	Inverter Side ($\hat{K}, \hat{\alpha}$)
Internal fault in the line area	400	10	(7, 173)	(6, 78)
		100	(6, 345)	(5, 89)
		300	(6, 107)	(5, 35)
	700	10	(4, 341)	(5, 183)
		100	(4, 210)	(4, 155)
		300	(4, 97)	(4, 104)
	1300	10	(7, 241)	(8, 541)
		100	(6, 99)	(8, 346)
		300	(6, 153)	(7, 301)
External fault on rectifier valve side	–	10	(10, 2251)	(9, 211)
	–	100	(11, 1544)	(9, 194)
External fault on inverter valve side	–	10	(8, 351)	(10, 658)
	–	100	(8, 222)	(9, 514)
Three-phase failure of the AC bus on the rectifier side	–	–	(9, 189)	(7, 58)
Three-phase fault of the AC bus on the inverter side	–	–	(7, 115)	(7, 258)

3.3. Directional Determination Based on Phase Angle Difference of Hilbert Transform

According to the analysis in Section 2.2, it can be shown that the residual components $r_R(t)$ and $r_I(t)$, which are obtained after the two-terminal current fault component Δi_R and Δi_I are decomposed by the VMD, can characterize the mutation direction of the fault signal. Therefore, taking the conclusion of Section 2.1 as a reference, it is proposed to utilize the Hilbert phase angle difference of the residual components of the current fault component at both ends to reflect the difference in the direction of the current fault component after a fault, and to take the Hilbert phase angle difference as a characteristic quantity for discriminating faults inside and outside the line area. Figure 3 shows the Hilbert transform results of the residual components $r_R(t)$ and $r_I(t)$ at both ends for faults inside and outside the DC line area, and the fault types are consistent with Section 2.2.

The residual components obtained after the Hilbert transform have better time-frequency resolution characteristics, which can provide complete transient information with good identification accuracy. It can be seen from Figure 3 that the monotonicity of the residual component affects the size of the Hilbert phase angle. For internal fault, the difference in Hilbert phase angles of the residual components calculated at both ends is small because the direction of the current fault component at both ends is positive and the transmission time of the data at both ends is taken into account. When an external fault occurs, the Hilbert phase angles of the residual components at the both ends obtained from subsequent calculations differ significantly due to the opposite direction of the current fault component at the both ends.

3.4. Directional Protection Criterion of the Current Fault Component Based on an Improved VMD-Hilbert Transform

There are four HVDC line protection devices, which are, respectively, installed at the beginning and end of the positive line and the beginning and end of the negative line. The line acquisition protection device obtains the current fault component at both ends of the positive and negative lines and the voltage fault component on the rectifier side of the positive and negative lines. The relevant criteria are defined as follows: the start criterion is the triggering condition of the protection process, the action criterion is the discriminating condition for recognizing internal and external faults, and the fault pole selection criterion is the discriminating condition for recognizing the faulty pole of the line.

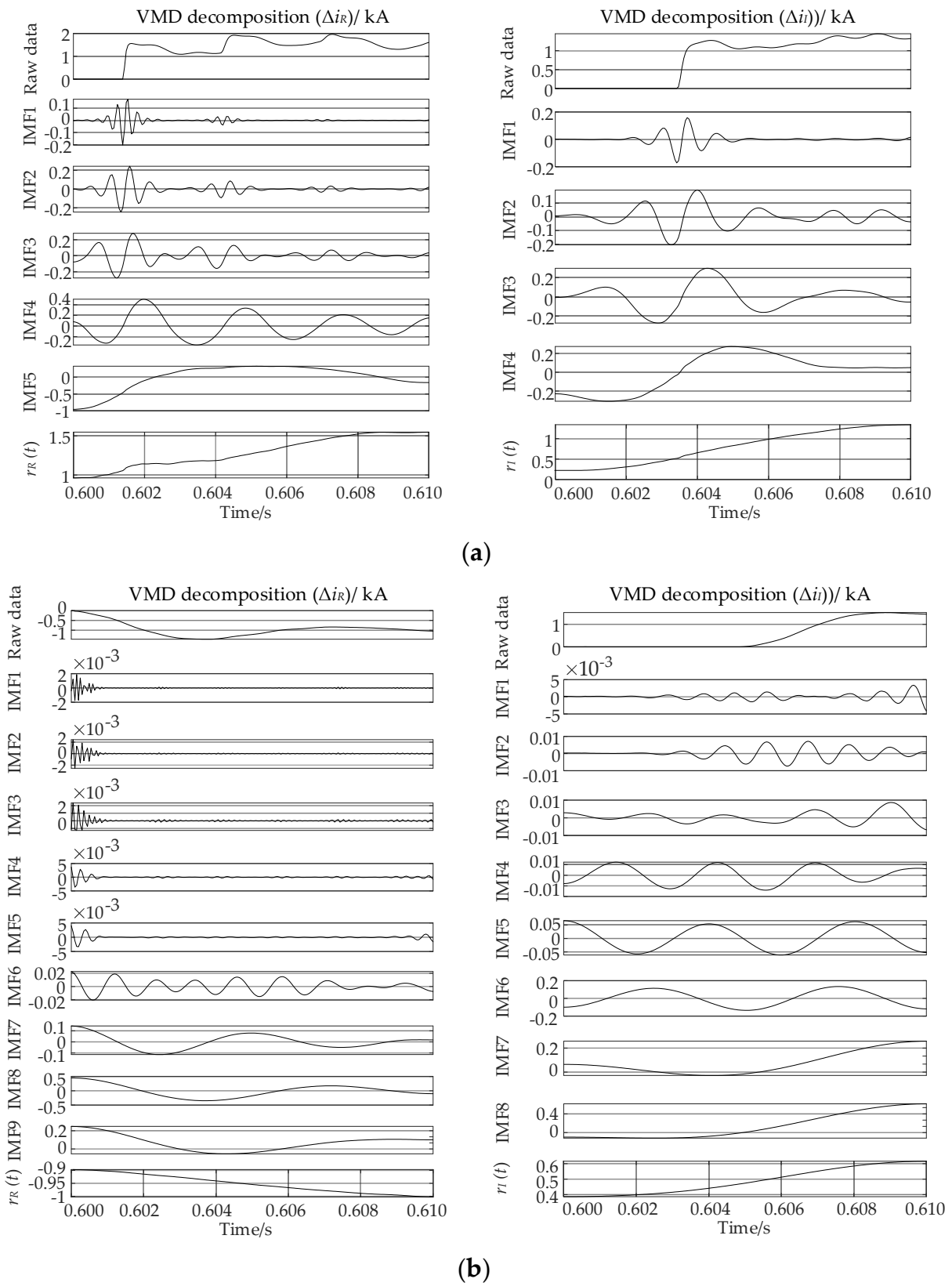


Figure 2. VMD waveform of faults inside and outside the line area. (a) VMD waveform of fault inside the line area; (b) VMD waveform of fault outside the line area.

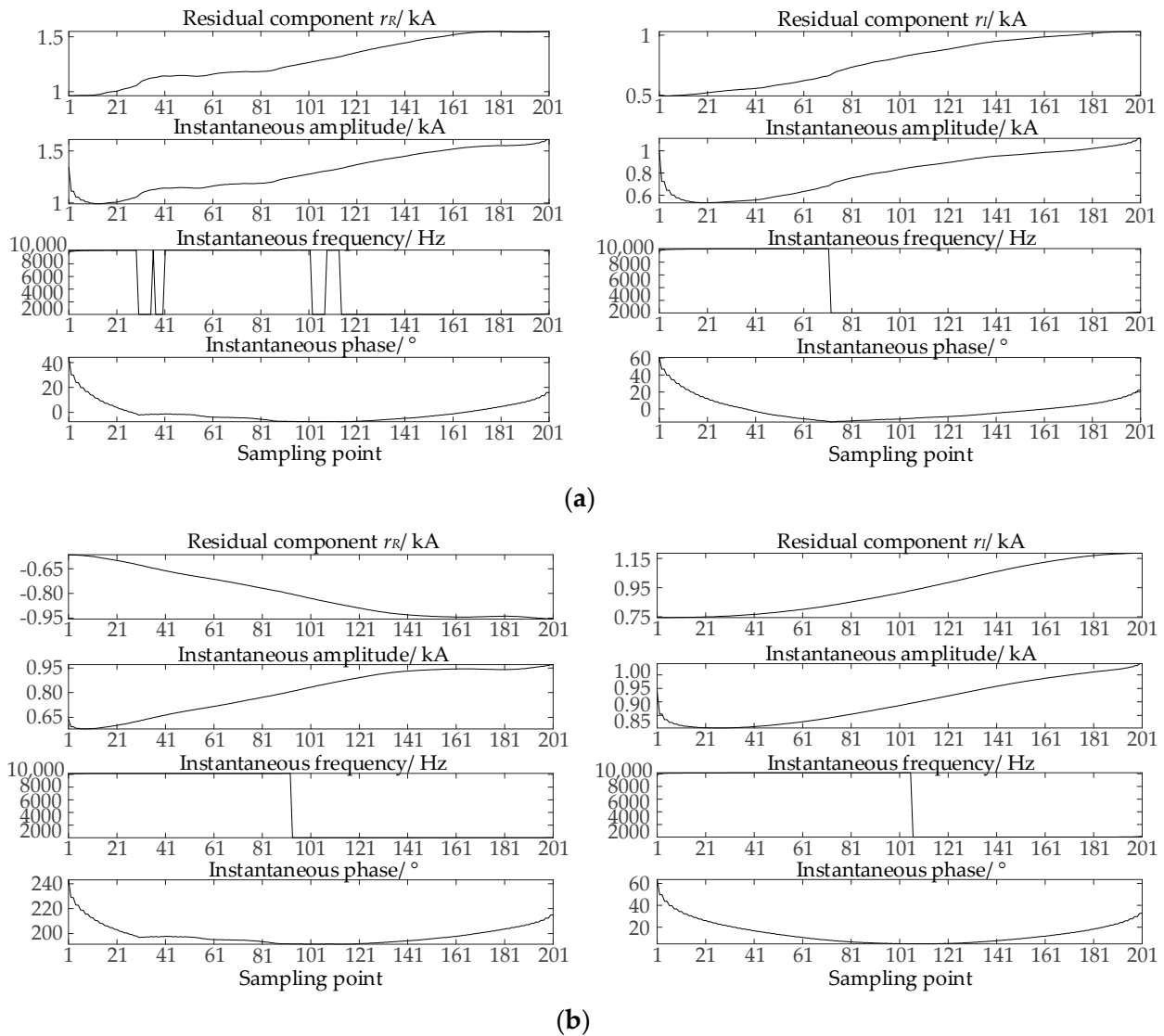


Figure 3. Hilbert transform diagram of faults inside and outside the line area. (a) Hilbert transform diagram of fault inside the line area; (b) Hilbert transform diagram of fault outside the line area.

1. Start criterion:

Construct a pole current protection activation criterion based on the value of the current fault component. Due to load and grid frequency fluctuations, the degree of fluctuation of the pole current is less than 8% of the rated current I_N during normal operation of the system. Let $I_{set} = 0.08I_N$, when the degree of fluctuation of the pole current Δi_φ is greater than the set current I_{set} , the protection is activated, as follows

$$\Delta i_\varphi > I_{set} \quad (21)$$

2. Action criterion:

From the above analysis, it is clear that the directional characteristics of the current components at both ends of the line are different when internal and external faults occur on the DC line. If the waveform of the fault transient signal is used directly to determine the direction, the protection may misjudge when lightning interference occurs, and it is difficult for the protection to cover the entire length of the line. In this regard, based on the theory in Section 1, it is proposed to utilize the improved VMD-Hilbert transform phase angle difference to discriminate the directional characteristics of the current fault component after

a fault, and then to identify whether or not an internal fault occurs in the line. The method first calculates the Hilbert phase angle of the current fault component for each sampling point in the data window and then finds the phase angle difference between both. In order to reduce the influence of interference and improve the stability of data analysis, the Hilbert phase angle difference at both ends was mean smoothed. After the discretization process, the action criterion of the protection is defined as

$$\Delta\theta_i = \frac{1}{N} \sum_{n=1}^N |\theta_{Ri}(n) - \theta_{Ii}(n)| \quad (22)$$

where: $i = 1, 2$ represents the positive and negative poles; $\theta_{Ri}(n)$, $\theta_{Ii}(n)$ represent the Hilbert phase angles of the current fault component of the rectifier side and the inverter side at the n -th sampling point on the i -pole, respectively and $\Delta\theta_i$ is the average of the absolute value of the difference of the Hilbert phase angles of both ends under the N sampling points.

According to Formula (22) and combined with the characterization of the direction of the current fault component in Section 2.1, it can be seen that the Hilbert phase angle difference between the residual component $r_R(t)$ and $r_I(t)$ at both ends during an internal fault is theoretically equal to 180° ; in the case of an external fault, the difference in phase angle between the both their phase angle difference is theoretically equal to 0° . In practice, considering the asynchronous transmission time of data at both ends, the protection needs to be set with sufficient margin to ensure reliable operation. Considering the sensitivity and reliability, the following criterion can be constructed

$$\begin{cases} \text{Internal fault : } & 0^\circ \leq \Delta\theta_i \leq 50^\circ \\ \text{External fault : } & 150^\circ \leq \Delta\theta_i \leq 200^\circ \end{cases} \quad (23)$$

In Formula (23), the protection only through the two-terminal fault quantities of the Hilbert phase angle difference of the direction of the discriminant value to identify the fault, the signal synchronization requirements are low, with a certain anti-interference ability, compared with the traditional time-frequency analysis method has a better adaptive resolution ability.

3. Fault pole selection criterion

For the bipolar DC system, when a single pole fault occurs on the overhead line, the voltage and current fault components are also detected on the sound pole due to the electromagnetic coupling between the two poles of the line, and the method of selecting the fault poles cannot be realized by using only the Hilbert phase angle difference. This paper introduces the method of identifying faulty poles using only the voltage fault component signal. Theory and simulation show that the energy of the post-fault voltage fault component is mainly concentrated in the low-frequency band, and the coupling coefficient of the two poles of the line is the largest when the frequency is 500~2000 Hz [33]. Due to the frequency-varying nature of the series impedance and shunt conductance of the transmission line, the high-frequency energy of the voltage fault component is greater than that of the sound pole. From this, a pole selection criterion can be constructed using the ratio of the high- and low-frequency Hilbert energy sums of the positive and negative single-ended voltage fault components. Figures A2 and A3 of Appendix B show the multi-band Hilbert instantaneous energy diagrams of voltage fault component on the rectifier side of the positive and negative poles during internal and external faults on the DC line, respectively, and the fault types are the same as in Section 2.2. The pole selection factor P is defined as

$$P = \frac{E_{R11} + E_{Rh1}}{E_{R12} + E_{Rh2}} = \frac{E_{R1}}{E_{R2}} \quad (24)$$

where E_{Rl1} , E_{Rh1} are the low-frequency Hilbert energy (1~500 Hz) and high-frequency Hilbert energy (6~10 kHz) of the voltage fault component on the positive rectifier side of the line; E_{Rh2} , E_{Rl2} are the high and low-frequency Hilbert energy of the voltage fault component on the negative rectifier side of the line; and E_{R1} , E_{R2} are the sum of the high and low-frequency Hilbert energy of the voltage fault component on the positive and negative rectifier sides of the line, respectively.

From this, a multi-band Hilbert energy sum ratio based on the positive and negative single-ended voltage fault component can be constructed as a fault pole selection criterion, expressed as follows

$$\begin{cases} \text{positive fault : } & P \geq P_{\text{set1}} \\ \text{negative fault : } & P \leq P_{\text{set2}} \\ \text{bipolar fault : } & P_{\text{set2}} \leq P \leq P_{\text{set1}} \end{cases} \quad (25)$$

where P_{set1} and P_{set2} are the upper and lower thresholds of the criterion, considering a certain margin, P_{set1} takes the value of 1.2, and P_{set2} takes the value of 0.95.

Summarizing the above, the two-terminal protection method for HVDC lines based on the improved VMD-Hilbert current fault component direction proposed in this paper is shown in Figure 4.

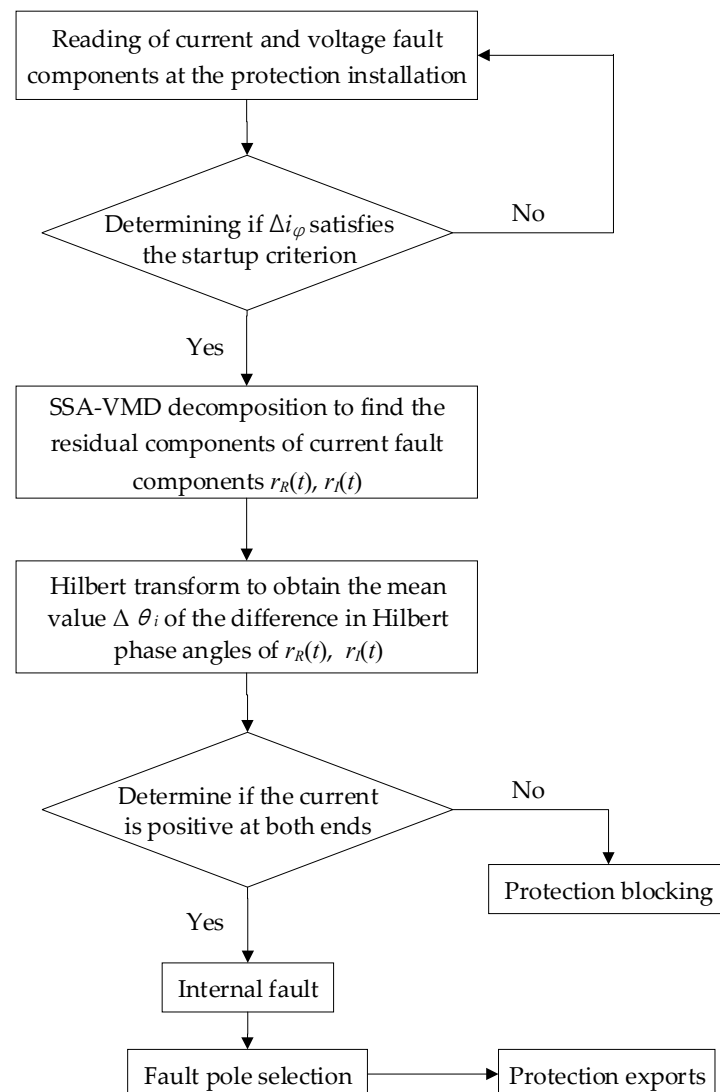


Figure 4. Flow chart of the two-terminal protection scheme.

4. Simulation Analysis of the Experiments

4.1. Simulation Model of the HVDC Transmission System

According to the actual parameters of the Yunnan-Guangzhou ± 800 kV Ultra-HVDC transmission system, a simulation model of the bipolar HVDC system shown in Figure 5 is constructed in PSCAD/EMTDC, with a voltage level of ± 800 kV and a rated current of 3.125 kA. Both the rectifier and inverter stations have a rated capacity of 2000 MW and use 12-pulse wave converter valves; the line is modeled in the frequency modal domain, with a total length of 1418 km and 6 splits; the rectifier station adopts constant current and constant trigger angle control, while the inverter station adopts constant current and constant arc quenching angle control, and at the same time, low voltage current limiting modules are installed at both ends.

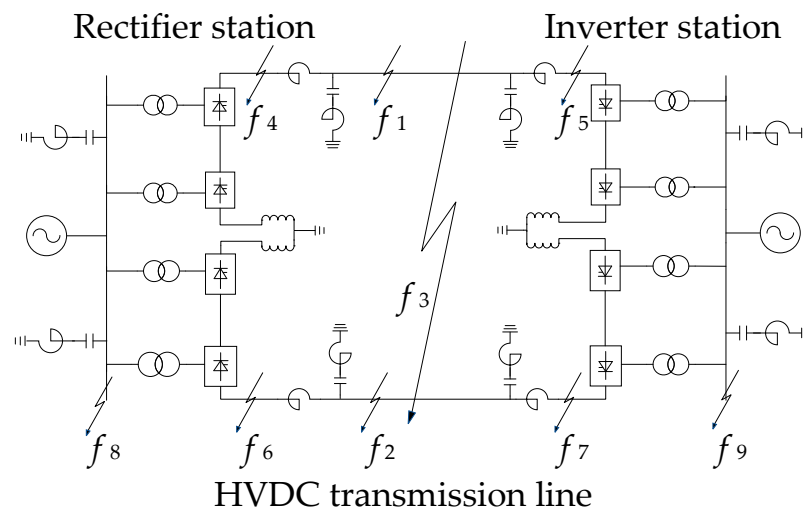


Figure 5. Configuration of the bipolar ± 800 kV HVDC Transmission system.

In Figure 5, f_1 and f_2 are positive and negative DC line internal faults; f_3 is a bipolar fault; f_4 and f_6 are positive and negative rectifier valve-side faults; f_5 and f_7 are positive and negative inverter valve-side faults; and f_8 and f_9 are three-phase short-circuit faults on the AC bus. In this paper, the simulation analysis sets the fault moment as $t = 0.6$ s, the time window length as 10 ms, the sampling frequency as 20 kHz, and the simulation analysis is carried out for different fault types using SSA-VMD and Hilbert transform.

4.2. Simulation of Internal Faults in the Line Area

The current fault component, residual components, and their Hilbert phase angle results of both ends of the rectifier and inverter sides at the positive line are shown in Figures 6 and 7, respectively, when the DC line has a f_1 positive ground fault (transition resistance of 100Ω) and a f_3 bipolar fault (transition resistance of 10Ω) at 400 km. The residual components of the current fault component at both ends at the positive line are characterized in the positive direction during the 10 ms time window after the fault, consistent with the analysis in Section 2.1.

The Hilbert phase angle difference can be calculated based on the Hilbert phase angle of the current fault component at each sampling point under the fault and combining it with Formula (22). In Figure 6, the Hilbert phase angle difference $\Delta\theta_1$ of the residual components at both ends is 4.7553° , and the multi-band Hilbert energy sums of E_{R1} and E_{R2} of the voltage fault component at the positive and negative rectifier sides are 3.1623×10^7 and 5.9243×10^5 , respectively, and then the identification factor P can be obtained to be 53.3783, which fulfills the positive pole fault action criterion. In Figure 7, the Hilbert phase angle difference $\Delta\theta_1$ of the residual components at both ends is 3.6599° , E_{R1} and E_{R2} are 4.1404×10^7 and 4.1165×10^7 , respectively, which calculates P to be 1.0058, and the protection is determined to be a bipolar fault.

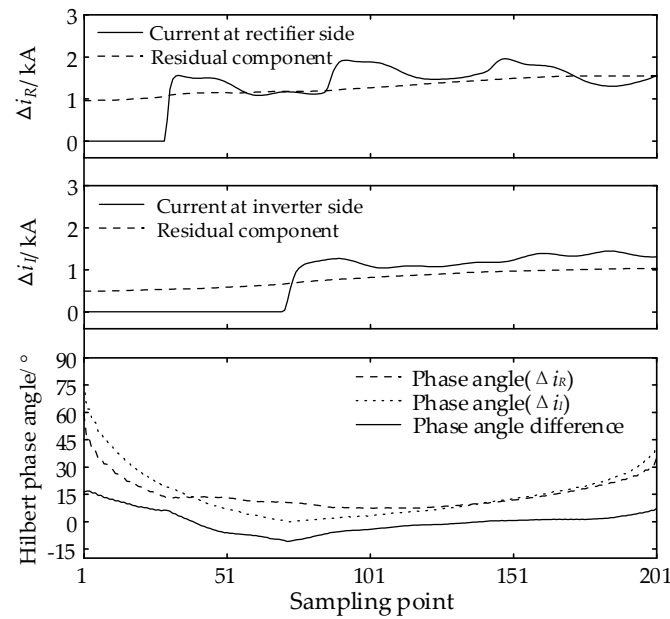


Figure 6. VMD-Hilbert angle curves for a fault at f_1 .

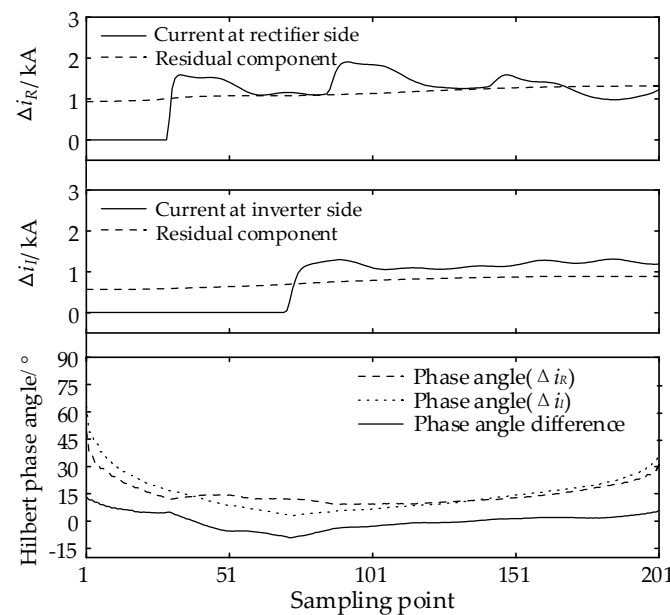


Figure 7. VMD-Hilbert angle curves for a fault at f_3 .

When an internal fault occurs in the negative line, the effects of different fault distances and different transition resistances on fault identification are examined, as shown by the simulation results in Table 2:

- (1) Under different fault distances and transition resistances, the protection can correctly determine the fault section and fault pole.
- (2) The Hilbert phase angle difference $\Delta\theta_2$ gradually increases from the midpoint of the line to both ends and when the distance to both ends is 100 km or less, the frequency oscillation of the current fault component causes $\Delta\theta_2$ to increase faster, which is significantly more on the rectifier side than on the inverter side.
- (3) SSA-VMD of the current fault component eliminates the effects of line distribution capacitance and communication noise, and reliably identifies faults at both ends of the line.

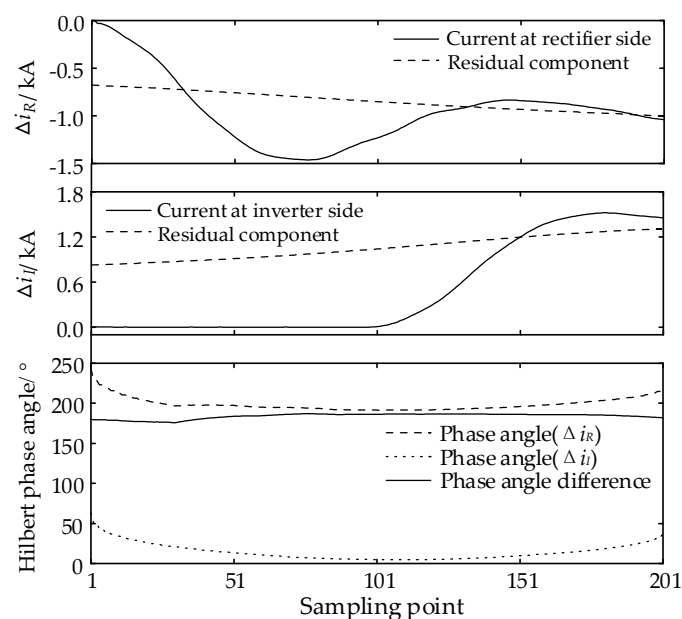
Table 2. Simulation results of faults on the negative line.

Fault Position	Transition Resistance/ Ω	Hilbert Phase Angle Difference $\Delta\theta_2/^\circ$	Electrode Selection Factor P	Identification Result
20 km	10	38.0279	0.0416	Negative internal fault
	100	36.4295	0.0223	Negative internal fault
	300	34.1124	0.0719	Negative internal fault
100 km	10	26.7622	0.0693	Negative internal fault
	100	25.2729	0.0545	Negative internal fault
	300	23.6231	0.0414	Negative internal fault
300 km	10	14.1787	0.0294	Negative internal fault
	100	22.5746	0.0202	Negative internal fault
	300	22.4879	0.0583	Negative internal fault
700 km	10	1.0162	0.0192	Negative internal fault
	100	0.1877	0.0361	Negative internal fault
	300	0.3662	0.0682	Negative internal fault
1300 km	10	13.3134	0.0634	Negative internal fault
	100	12.8028	0.1125	Negative internal fault
	300	18.3977	0.1265	Negative internal fault

4.3. Simulation of External Faults in the Line Area

Figures 8 and 9 show the simulation results of the current fault component, residual components, and their Hilbert phase angles at both ends of the DC line for the positive rectifier valve side fault f_4 and the inverter valve side fault f_5 , respectively. The Hilbert phase angle difference $\Delta\theta_1$ of the residual components at both ends during the external fault is 185.2359° and 190.1289° , respectively, showing opposite polarity, which satisfies the condition of external fault discrimination.

In order to test the effect of different transition resistances on fault identification during an external fault, the positive rectifier valve side and the inverter valve side are set up to experience external faults f_4 and f_5 , as well as the three-phase faults f_8 and f_9 at the AC bus, which are set up to have transition resistances of 10Ω , 100Ω , and 300Ω at the point of the faults, respectively. Table 3 shows the Hilbert phase angle differences detected at both ends of the positive and negative lines and the results of the determination.

**Figure 8.** VMD-Hilbert angle curves for a fault at f_4 .

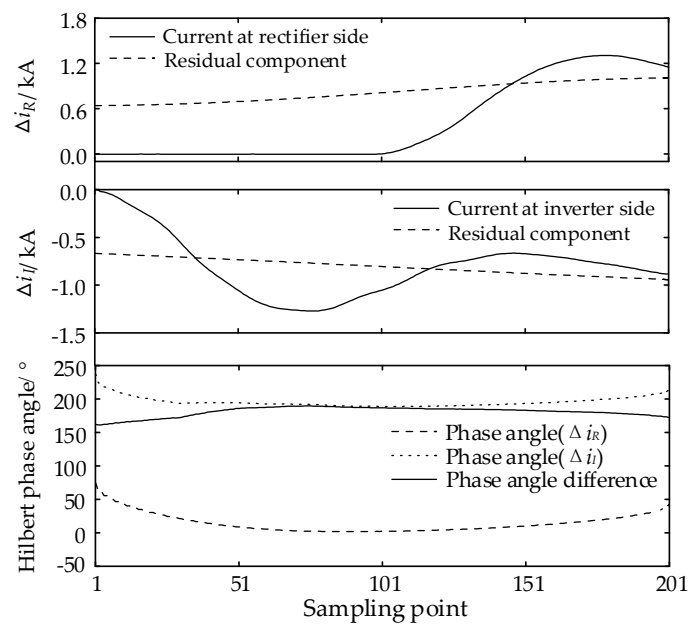


Figure 9. VMD-Hilbert angle curves for a fault at f_5 .

Table 3. Simulation results of external faults.

Fault Position	Transition Resistance/ Ω	Hilbert Phase Angle Difference $\Delta\theta_1/^\circ$	Hilbert Phase Angle Difference $\Delta\theta_2/^\circ$	Identification Result
f_4	10	185.2359	173.6549	External fault
	100	187.3681	177.6515	External fault
	300	182.8825	173.3255	External fault
f_5	10	182.1298	170.6549	External fault
	100	181.8433	176.2542	External fault
	300	180.5513	178.9875	External fault
f_8	–	183.4566	176.4587	External fault
f_9	–	181.1287	173.5422	External fault

Due to the high-frequency resistive-band transmission characteristics at the line boundary, the waveforms of the current fault component measured at both ends are smooth, and the two sets of residual components decomposed by the SSA-VMD during external faults are highly directional and show opposite polarities. At the same time, the corresponding Hilbert phase angle is detected on both sides of the sounding pole by the electromagnetic coupling between the DC lines. From the simulation results in Table 3, it can be seen that $\Delta\theta_1$ and $\Delta\theta_2$ are both in the $150^\circ \sim 200^\circ$ interval, and none of the protections will operate incorrectly, which does not affect the fault recognition of this protection.

4.4. Examination of Anti-Noise Interference Performance

In the DC line, two-terminal quantities may introduce noise during transmission over long communication channels. In order to check the noise immunity of the proposed protection scheme, a white noise signal with a signal-to-noise ratio of 10 dB is superimposed on the original current mutation signal. The fault types are set as f_1 positive ground fault (transition resistance of 100 Ω) and f_4 rectifier valve side fault (transition resistance of 10 Ω) in the DC line at 400 km, respectively. From Figures 10 and 11, it can be seen that the white noise signal will cause fluctuations in the amplitude of the fault current, which only exists in the high-level IMF component after VMD, and the trend of the residual component is less affected, and if the parameters of the VMD algorithm are properly selected, the residual component still has the pointing characteristics that characterize the direction of

the current fault component. Under the fault condition of superimposed noise interference, the Hilbert phase angle difference $\Delta\theta_1$ of the residual components at both ends is sought to be 9.9437° and 170.9437° , respectively, and the protection can still reliably discriminate internal and external faults. Therefore, the double-ended protection method proposed in this paper can effectively filter out the fluctuations through SSA-VMD and has certain anti-noise interference capabilities.

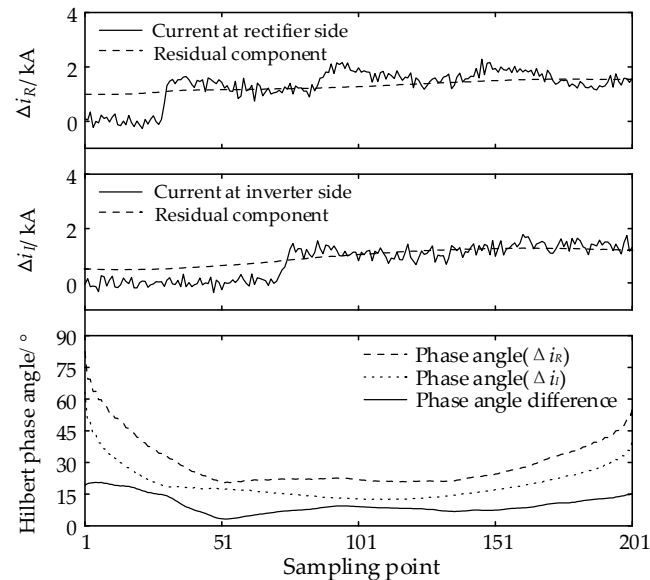


Figure 10. VMD-Hilbert angle curves for a fault at f_1 .

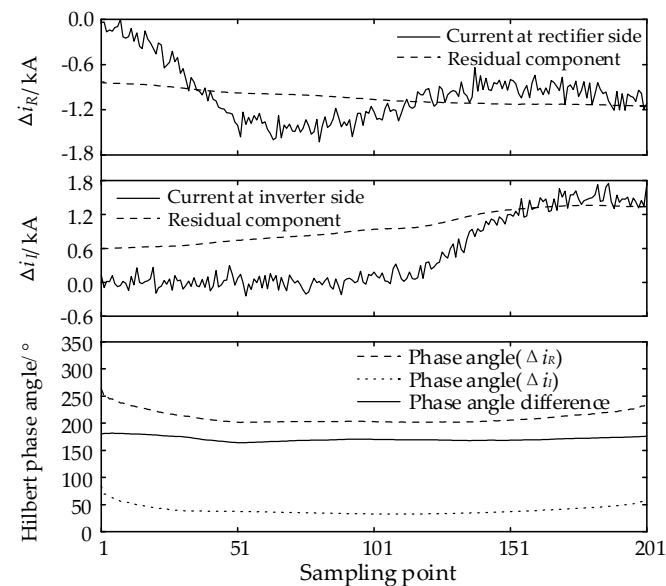


Figure 11. VMD-Hilbert angle curves for a fault at f_4 .

4.5. Analysis of Protection Action Time

The two-terminal protection action time is mainly composed of three parts: traveling wave conveyance time difference, channel communication delay, and algorithm calculation time. For a 1418 km long transmission line, the wave speed of the fault traveling wave is approximated to be 98% of the speed of light, and the maximum time difference of the traveling wave conveyed to the measurement points at both ends is about 4.8 ms. In terms of communication delay, the signal transmission rate of dedicated optical fiber communication is about $4.9 \mu\text{s}/\text{km}$, so the transmission delay of the 1418-km-long optical

fiber longitudinal link channel is about 6.9 ms. The algorithm computation time consists of a 10 ms data time window with 0.5 ms computation time, which is approximately 10.5 ms. Taking the above analysis into account and considering the appropriate margin, the total action time of the protection system is about 23 ms, which is earlier than the action time of the control system (about 30 ms) and much faster than that of the current differential protection considering the influence of the distributed capacitance current (about 1100 ms) and can better satisfy the requirement of the backup protection of the DC line.

5. Conclusions

This paper proposes a two-terminal current fault component directional protection based on SSA-VMD and Hilbert transform phase angle difference. The feasibility of this protection scheme is evaluated through theoretical analysis and simulation verification, and the results show that this method has the following characteristics:

- (1) VMD combines the features of SSA solving speed and selects the average envelope entropy as the fitness function to adaptively determine the best selection parameters of VMD, which effectively solves the problem of difficult selection of VMD parameters. Nevertheless, optimization for large-scale complex problems should also be evaluated and tuned on a case-by-case basis.
- (2) SSA-VMD can eliminate the influence of line distributed capacitance and communication noise on the current fault component at both ends of the line, obtain the residual component characterizing the direction of change at both ends, and then calculate the Hilbert phase angle difference through Hilbert transform to determine the directional relationship of the current fault component at both ends of the line. Meanwhile, the ratio of multi-band Hilbert energy sum of single-ended voltage fault component at both poles can be obtained by improving the VMD-Hilbert transform to effectively identify the fault poles.
- (3) Compared with the existing DC differential protection and pilot protection, the proposed protection is not affected by the distributed capacitance and does not depend on the boundary conditions. As verified by simulation, the method does not require a high sampling device and has fast action speed, can reliably identify the internal and external faults, has good tolerance to transition resistance and anti-noise interference, and better meets the backup protection needs of HVDC transmission lines.
- (4) The two-terminal backup protection method proposed in this paper can also be used as the main protection without considering the communication delay and the calculation amount, and can be combined with each other for further analysis in the future. Since the scheme is based on theoretical analysis and simulation verification, it needs to be further combined with actual engineering to verify the applicability of the scheme. At the same time, based on the research in this article, further research can be conducted on this method in related fields of power systems such as lightning strike identification, fault location, fault intelligent algorithm, transient signal analysis, and power quality analysis.

Author Contributions: Conceptualization, S.L. and K.H.; methodology, S.L.; software, S.L.; validation, S.L., H.L. and T.Z.; formal analysis, S.L.; investigation, K.H.; resources, K.H.; data curation, S.L.; writing—original draft preparation, S.L.; writing—review and editing, H.L.; visualization, T.Z.; supervision, F.C.; project administration, H.L.; funding acquisition, K.H. All authors have read and agreed to the published version of the manuscript.

Funding: This research was funded by The National Natural Science Foundation of China (Funder: Kunlun Han; No. 51567003).

Data Availability Statement: The data presented in this study are available in insert article.

Conflicts of Interest: The authors declare no conflict of interest. The funders had no role in the design of the study; in the collection, analyses, or interpretation of data; in the writing of the manuscript; or in the decision to publish the results.

Appendix A

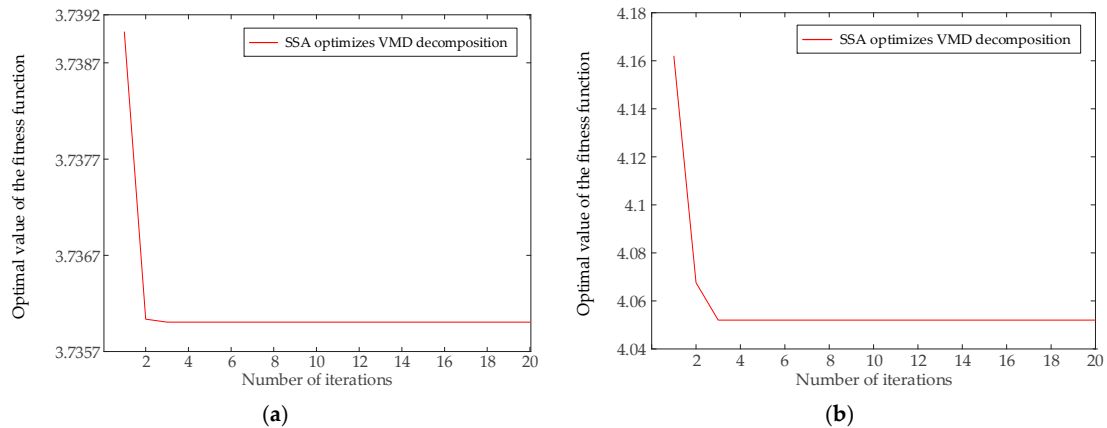


Figure A1. Curve of the optimization value and iteration times of SSA for an internal fault. (a) Optimization of SSA parameters for Δi_R ; (b) Optimization of SSA parameters for Δi_L .

Appendix B

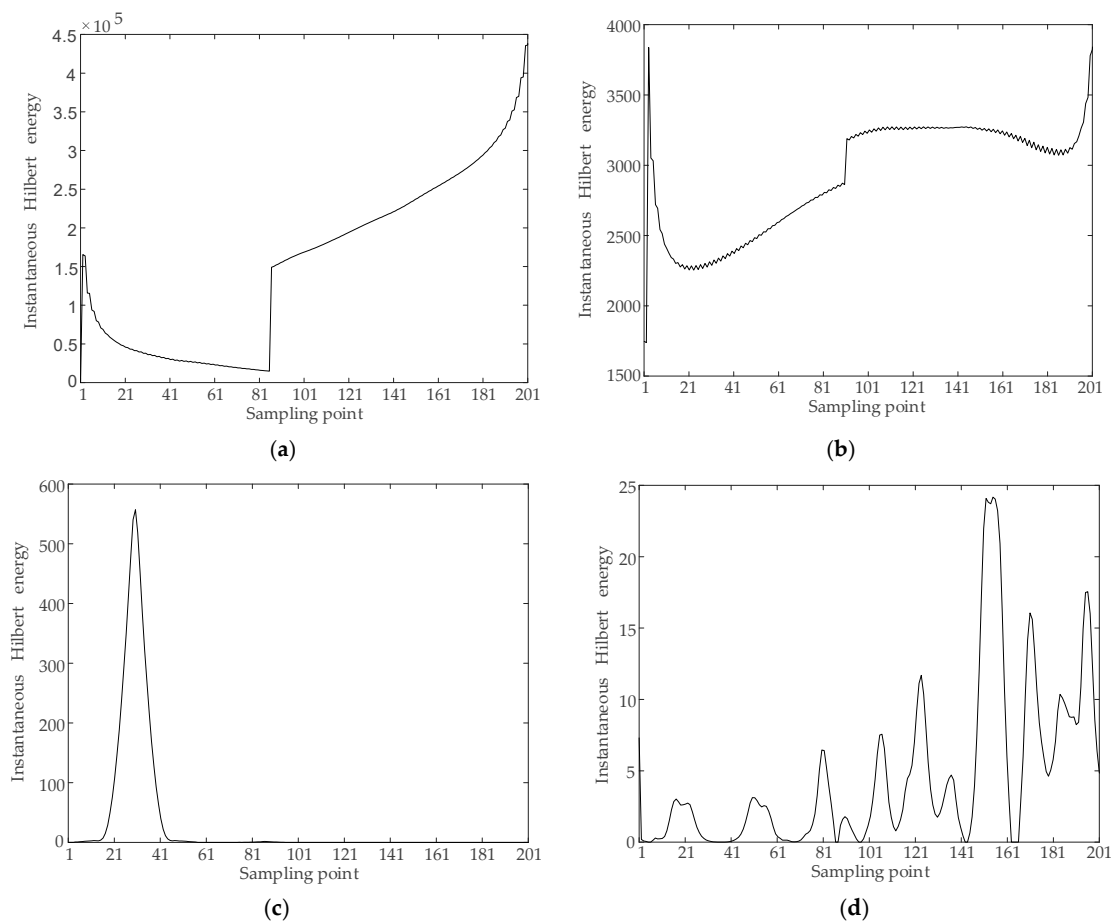


Figure A2. Multi-band Hilbert instantaneous energy diagrams of voltage fault component at the positive and negative rectifier sides during an internal fault in the line. (a) Positive pole voltage fault component of the internal fault 1~500 Hz low-frequency band Hilbert instantaneous energy; (b) Negative pole voltage fault component of the internal fault 1~500 Hz low-frequency band Hilbert instantaneous energy; (c) Positive voltage pole fault component of the internal fault 6000~10,000 Hz high-frequency band Hilbert instantaneous energy; (d) Negative pole voltage fault component of the internal fault 6000~1000 Hz high-frequency band Hilbert instantaneous energy.

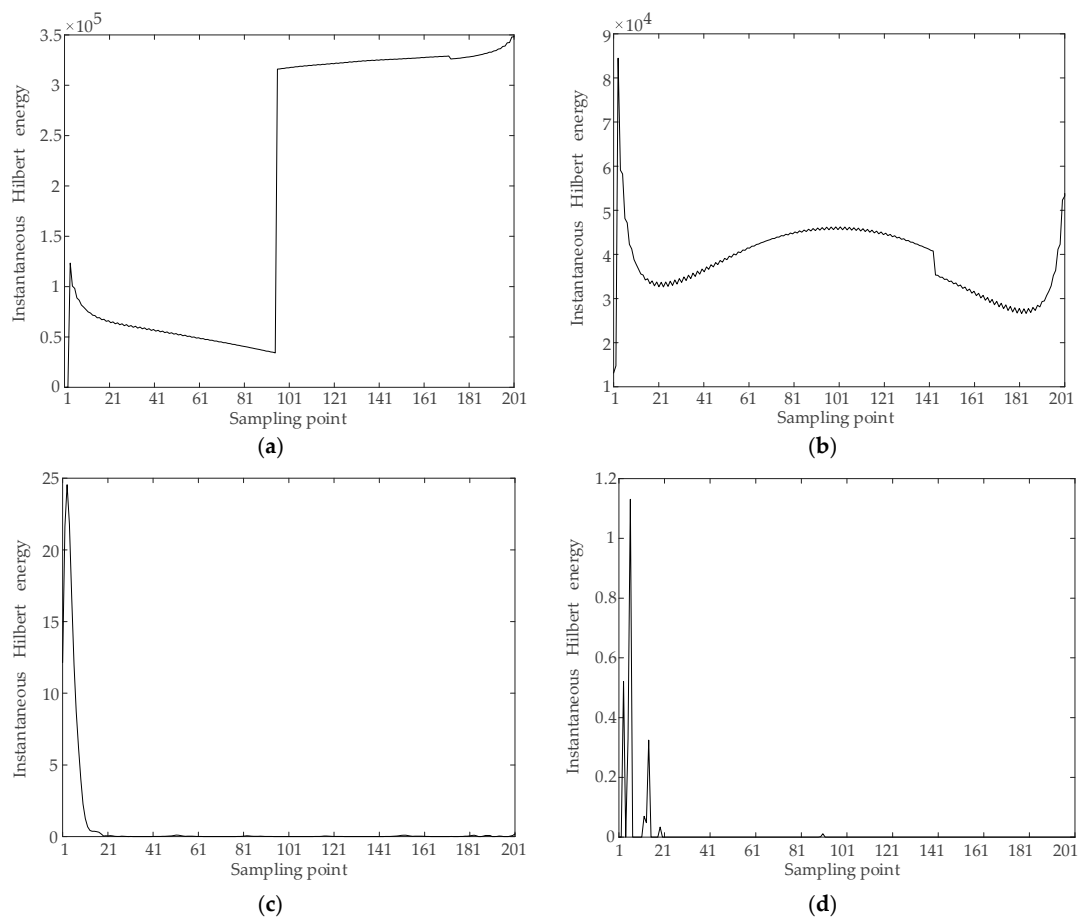


Figure A3. Multi-band Hilbert instantaneous energy diagrams of voltage fault component at the positive and negative rectifier sides during an external fault in the line. (a) Positive pole voltage fault component of the external fault 1~500 Hz low-frequency band Hilbert instantaneous energy; (b) Negative pole voltage fault component of the external fault 1~500 Hz low-frequency band Hilbert instantaneous energy; (c) Positive voltage pole fault component of the external fault 6000~10,000 Hz high-frequency band Hilbert instantaneous energy; (d) Negative pole voltage fault component of the external fault 6000~1000 Hz high-frequency band Hilbert instantaneous energy.

References

- Perez-Molina, M.J.; Larruskain, D.M.; Lopez, P.E.; Buigues, G.; Valverde, V. Review of Protection Systems for Multi-terminal High Voltage Direct Current Grids. *Renew. Sustain. Energy Rev.* **2021**, *144*, 111037.
- Radwan, M.; Azaz, S.P. Protection of Multi-Terminal HVDC Grids: A Comprehensive Review. *Energies* **2022**, *15*, 9552.
- Bahrman, M.P.; Johnson, B.K. The ABCs of HVDC Transmission Technologies. *IEEE Power Energy Mag.* **2007**, *5*, 32–44. [[CrossRef](#)]
- Muniappan, M. A comprehensive Review of DC Fault Protection Methods in HVDC Transmission Systems. *Prot. Control. Mod. Power Syst.* **2021**, *6*, 1.
- Zhang, Y.; Tai, N.L.; Xu, B. Fault Analysis and Traveling-Wave Protection Scheme for Bipolar HVDC Lines. *IEEE Trans. Power Deliv.* **2012**, *27*, 1583–1591. [[CrossRef](#)]
- Gao, B.F.; Zhang, R.X.; Zhang, X.W. A Novel Procedure for Protection Setting in an HVDC System Based on Fault Quantities. *J. Electr. Eng. Technol.* **2017**, *12*, 513–521. [[CrossRef](#)]
- Gao, S.P.; Liu, Q.; Song, G.B. Current Differential Protection Principle of HVDC Transmission System. *IET Gener. Transm. Distrib.* **2017**, *11*, 1286–1292. [[CrossRef](#)]
- Lin, S.; Gao, S.; He, Z.Y.; Deng, Y.J. A Pilot Directional Protection for HVDC Transmission Line Based on Relative Entropy of Wavelet Energy. *Entropy* **2015**, *17*, 5257–5273. [[CrossRef](#)]
- Li, Z.; Zou, G.B.; Du, T.; Yang, W.J. S-Transform Based Pilot Protection Method for HVDC Transmission Lines. In Proceedings of the 2015 5th International Conference on Electric Utility Deregulation and Restructuring and Power Technologies, Changsha, China, 26–29 November 2015; pp. 1667–1672.
- Shu, H.C.; Tian, X.C. Entire-line Instant Protection Based on PCA Clustering for 800kV HVDC Transmission Line. *Electr. Power Autom. Equip.* **2016**, *36*, 51–59.

11. Gong, Y.L.; Cao, B.H.; Zhang, H.; Sun, F.S.; Fan, M.B. Terahertz Based Thickness Measurement of Thermal Barrier Coatings Using Hybrid Machine Learning. *Nondestruct. Test. Eval.* **2023**, *47*, 1–18. [[CrossRef](#)]
12. Weingessel, A.; Hornik, K. Local PCA Algorithms. *IEEE Trans. Neural Netw.* **2000**, *11*, 1242–1250. [[PubMed](#)]
13. Qi, G.Q.; Wang, Z.P. Directional Pilot Protection Method of Fault Component for HVDC Transmission Lines Based on Hilbert-Huang Transform. *Power Syst. Prot. Control.* **2017**, *45*, 92–99.
14. Liu, Z.G.; Gui, Y.; Li, W.H. A Classification Method for Complex Power Quality Disturbances Using EEMD and Rank Wavelet SVM. *IEEE Trans. Smart Grid* **2015**, *6*, 1678–1685. [[CrossRef](#)]
15. Zhan, L.W.; Li, C.W. A Comparative Study of Empirical Mode Decomposition-Based Filtering for Impact Signal. *Entropy* **2016**, *19*, 13. [[CrossRef](#)]
16. Dragomiretskiy, K.; Zosso, D. Variational Mode Decomposition. *IEEE Trans. Signal Process.* **2014**, *62*, 531–544. [[CrossRef](#)]
17. Salim, L. Comparative Study of ECG Signal Denoising by Wavelet Thresholding in Empirical and Variational Mode Decomposition Domains. *Healthc. Technol. Lett.* **2014**, *1*, 104–109.
18. Wang, Y.X.; Markert, R.; Xiang, J.W. Research on Variational Mode Decomposition and its Application in Detecting Rub-impact Fault of the Rotor System. *Mech. Syst. Signal Process.* **2015**, *60*, 243–251. [[CrossRef](#)]
19. Yang, H.B.; Liu, S.L.; Zhang, H.L. Adaptive Estimation of VMD Modes Number Based on Cross Correlation Coefficient. *J. Vibroengineering* **2017**, *19*, 1185–1196. [[CrossRef](#)]
20. Viswanath, A.; Jose, K.J.; Krishnan, N.; Kumar, S.S.; Soman, K.P. Spike Detection of Disturbed Power Signal Using VMD. *Procedia Comput. Sci.* **2015**, *46*, 1087–1094. [[CrossRef](#)]
21. Wang, L.; Liu, H.; Dai, L.V.; Liu, Y.W. Novel Method for Identifying Fault Location of Mixed Lines. *Energies* **2018**, *11*, 1529. [[CrossRef](#)]
22. Xu, Y.C.; Gao, Y.K.; Li, Z.H.; Lu, M. Detection and Classification of Power Quality Disturbances in Distribution Networks Based on VMD and DFA. *Csee J. Power Energy Syst.* **2019**, *6*, 122–130.
23. Luo, D.R.; Wu, T.; Li, M.; Yi, B.S.; Zuo, H.B. Application of VMD and Hilbert Transform Algorithms on Detection of the Ripple Components of the DC Signal. *Energies* **2020**, *13*, 935. [[CrossRef](#)]
24. Wang, L.; He, Y.G.; Li, L. A Single-Terminal Fault Location Method for HVDC Transmission Lines Based on a Hybrid Deep Network. *Electronics* **2021**, *10*, 255. [[CrossRef](#)]
25. Song, S.D.; Yao, Z.C.; Wang, X.N. The summary of Hilbert-Huang transform. In Proceedings of the 2013 5th International Symposium on Photoelectronic Detection and Imaging (ISPD)—Infrared Imaging and Applications, Beijing, China, 25–27 June 2013.
26. Paternina, M.R.A.; Tripathy, R.K.; Zamora-Mendez, A.; Dotta, D. Identification of Electromechanical Oscillatory Modes Based on Variational Mode Decomposition. *Electr. Power Syst. Res.* **2019**, *167*, 71–85. [[CrossRef](#)]
27. Xiao, G.; Xu, F.; Tong, L.H.; Xu, H.R.; Zhu, P.W. A Hybrid Energy Storage System Based on Self-adaptive Variational Mode Decomposition to Smooth Photovoltaic Power Fluctuation. *J. Energy Storage* **2022**, *55*, 105509. [[CrossRef](#)]
28. Zhang, Q.; Ma, W.H.; Li, G.L.; Ding, J.J.; Xie, M. Fault Diagnosis of Power Grid Based on Variational Mode Decomposition and Convolutional Neural Network. *Electr. Power Syst. Res.* **2022**, *208*, 107871. [[CrossRef](#)]
29. Yue, Y.G.; Cao, L.; Lu, D.W.; Hu, Z.Y.; Xu, M.H. Review and Empirical Analysis of Sparrow Search Algorithm. *Artif. Intell. Rev.* **2023**, *56*, 10867–10919.
30. Yan, X.A.; Jia, M.P.; Xiang, L. Compound Fault Diagnosis of Rotating Machinery Based on OVMD. *Meas. Sci. Technol.* **2016**, *27*, 075002. [[CrossRef](#)]
31. Zhang, X.; Sun, T.T.; Wang, Y.; Wang, K.W.; Shen, Y. A Parameter Optimized Variational Mode Decomposition Method for Rail Crack Detection Based on Acoustic Emission Technique. *Nondestruct. Test. Eval.* **2020**, *36*, 411–439. [[CrossRef](#)]
32. Zheng, X.X.; Wang, S.; Qian, Y.Q. Fault Feature Extraction of Wind Turbine Gearbox under Variable Speed Based on Improved Adaptive Variational Mode Decomposition. *Proc. Inst. Mech. Eng. Part A J. Power Energy* **2019**, *234*, 848–861. [[CrossRef](#)]
33. Song, G.B.; Chu, X.; Gao, S.P.; Kang, X.N.; Jiao, Z.B. A New Whole-Line Quick-Action Protection Principle for HVDC Transmission Lines Using One-end Current. *IEEE Trans. Power Deliv.* **2014**, *30*, 599–607. [[CrossRef](#)]

Disclaimer/Publisher’s Note: The statements, opinions and data contained in all publications are solely those of the individual author(s) and contributor(s) and not of MDPI and/or the editor(s). MDPI and/or the editor(s) disclaim responsibility for any injury to people or property resulting from any ideas, methods, instructions or products referred to in the content.